The Astrophysical Journal, 849:16 (13pp), 2017 November 1 https://doi.org/10.3847/1538-4357/aa8d6c

X-Ray Timing Analysis of Cyg X-3 Using AstroSat/LAXPC: Detection of Milli-hertz Quasi-periodic Oscillations during the Flaring Hard X-Ray State

Mayukh Pahari[1], H M Antia[2], J S Yadav[2], Jai Verdhan Chauhan[2], P C Agrawal[3], Ranjeev Misra[1], V R Chitnis[2], Dhiraj Dedhia[2], Tilak Katoch[2], P Madhwani[2], R K Manchanda[4], B Paul[5], and Parag Shah[2]
[1] Inter-University Center for Astronomy and Astrophysics, Ganeshkhind, Pune 411007, India; mayukh@iucaa.in
[2] Tata Institute of Fundamental Research, Homi Bhabha Road, Mumbai 400005, India
[3] UM-DAE Center of Excellence for Basic Sciences, University of Mumbai, Kalina, Mumbai 400098, India
[4] University of Mumbai, Kalina, Mumbai 400098, India
[5] Department of Astronomy and Astrophysics, Raman Research Institute, Bengaluru 560080, India
Received 2017 January 26; revised 2017 July 25; accepted 2017 September 16; published 2017 October 25

Abstract

We present here results from the X-ray timing and spectral analysis of the X-ray binary Cyg X-3 using observations from the Large Area X-ray proportional Counter on board *AstroSat*. Consecutive light curves observed over a period of one year show the binary orbital period of 17253.56 ± 0.19 s. Another low-amplitude, slow periodicity of the order of 35.8 ± 1.4 days is observed, which may be due to the orbital precession as suggested earlier by Molteni et al. During the rising binary phase, power density spectra from different observations during the flaring hard X-ray state show quasi-periodic oscillations (QPOs) at ∼5–8 mHz, ∼12–14 mHz, and ∼18–24 mHz frequencies at the minimum confidence of 99%. However, during the consecutive binary decay phase, no QPO is detected up to 2σ significance. Energy-dependent time-lag spectra show soft lag (soft photons lag hard photons) at the mHz QPO frequency and the fractional rms of the QPO increases with the photon energy. During the binary motion, the observation of mHz QPOs during the rising phase of the flaring hard state may be linked to the increase in the supply of the accreting material in the disk and corona via stellar wind from the companion star. During the decay phase, the compact source moves in the outer wind region causing the decrease in supply of material for accretion. This may cause weakening of the mHz QPOs below the detection limit. This is also consistent with the preliminary analysis of the orbital phase-resolved energy spectra presented in this paper.

Key words: accretion, accretion disks – black hole physics – X-rays: binaries – X-rays: individual (Cyg X3)

1. Introduction

Discovered nearly 40 years ago (Giacconi et al. 1967), Cygnus X-3 is one of the brightest, persistent, and extraordinary Galactic high-mass X-ray binaries. The X-ray emission is driven by the wind accretion from the massive Wolf–Rayet companion star (∼20 $M_{\odot}$; Fender et al. 1999; Szostek & Zdziarski 2008; Vilhu et al. 2009) along with relatively bright persistent radio emission virtually all of the time (∼100 mJy) and occasionally accompanied by major radio ejection events of the order of 10 Jy or more (Molnar et al. 1988; Schalinski et al. 1995; Mioduszewski et al. 2001). The source resides close to the Galactic plane at a distance of 8–10 kpc (Dickey 1983). A strong X-ray flux modulation with a 4.8 hr cycle is observed (Parsignault et al. 1972; Leach et al. 1975; Kitamoto et al. 1989) and attributed to the binary orbital period of the system. The rate of change of the binary orbital period has been measured as $\sim 10^{-9}$ s s^{-1} (van der Klis & Bonnet-Bidaud 1981; Kitamoto et al. 1989). However, the binary orbital period derivative has been revised ($\sim 5 \times 10^{-10}$ s s^{-1}) by Singh et al. (2002) using multi-mission data spanning over seven years. Longer modulation in X-rays (∼34.1 days; Holt et al. 1976; Molteni et al. 1980) and in radio light curve (>60 days) are thought to be connected with the precessional motion of the accretion disk (Mioduszewski et al. 2001). In spite of extensive study, little is known about the compact nature of the source. Based on little evidence and similarities with black hole systems like GRS 1915+105, XTE J1550-564, the compact object is suggested to be a black hole (Szostek et al. 2008), which is yet to be confirmed. Linking *RXTE*/PCA observations to the simultaneous radio observations, Koljonen et al. (2010) studied the hardness intensity diagram (HID) and found six different spectral states. In addition to canonical spectral states of black hole X-ray binaries, they identified a hyper-soft spectral state/radio quenched state when strong GeV flux is detected using the Fermi telescope (Bodaghee et al. 2013).

The study of the X-ray spectra at different spectral states and its timing variability have suffered severely from the poor understanding of the properties of the surrounding medium. As a consequence, a detailed interpretation of the Cyg X-3 intrinsic unabsorbed spectrum and luminosity is still missing. Interestingly, Manchanda (2002) found that the number of X-ray photons in the 2–500 keV energy range is conserved irrespective of the source spectral state and such behavior is explained using an accretion geometry in which a thermal X-ray source is surrounded by hot plasma formed by the wind from the accretion disk. Based on simultaneous *INTEGRAL* and *RXTE* spectral modeling, Vilhu et al. (2003) interpreted the physical nature of X-ray emission as the strongly absorbed thermal Comptonization including Compton reflection and with parameters similar to other X-ray binaries at high accretion rates. Similar efforts are also given (e.g., Szostek & Zdziarski 2004; Zdziarski et al. 2010) to understand the nature of different accretion states in this peculiar source.

Despite the availability of large archival data from *RXTE*/PCA, the X-ray timing properties of Cyg X-3 are not particularly well studied. One reason could be the absence of high-frequency power in the power density spectra (PDS)

above 0.1 Hz (a result that has been discussed in Berger & van der Klis 1994, who placed an upper limit of 12% rms above 1 Hz)) where most of the other low-mass X-ray binaries show low- and high-frequency quasi-periodic oscillations (QPOs). This is believed to be an effect of scattering in the nearby surrounding medium (Zdziarski et al. 2010). The PDS from Cyg X-3 is well-described by a power law with the index between −1.8 (Willingale et al. 1985) and −1.5 (Choudhury & Rao 2004). QPOs from Cyg X-3 at the mHz frequency range have been reported few times in the literature. *EXOSAT*/ME observed 0.7–15 mHz QPOs in the PDS during the soft state with an rms amplitude between 5% and 15% (van der Klis & Jansen 1985). A balloon study (Rao et al. 1991; Manchanda & Rao 1993) showed a QPO in the 20–100 keV light curve with a frequency of 8 mHz (121 s) and a pulse fraction of 40%. However, contrary to these results, a study based on *RXTE* pointing data of Cyg X-3 from 1996–2000 (Axelsson et al. 2009) found no evidence of QPOs on any timescale. Specifically, on shorter timescales ($>10^{-3}$ Hz), no QPO is detected and the power density spectrum is well described by a power law of index −2 (which is typical of the red noise that essentially mimics a random walk process), while on the longer timescales ($<10^{-3}$ Hz), the variability is found to be dominated by the state transitions. The transient and time-sensitive nature of such QPOs could be a reason of discrepancy between results supporting the detection and nondetection of QPOs.

Koljonen et al. (2011) reanalyzed archival *RXTE* data of the X-ray binary Cyg X-3 and they identified two additional instances of QPOs above the 99.9% confidence limit, that have centroid frequencies in the mHz regime. The first one is detected at 8.5 mHz (∼120 s) on 2000 April 03, 2.2 days after the peak of a major radio flare (∼13 Jy in the 15 GHz band) when the source was in the flaring soft X-ray state (FSXR). During the flaring hard X-ray (FHXR) state observed on 2009 August 9, a strong 21 mHz (∼50 s) QPO was detected that corresponds to a 1.5%–2% rms in the PDS and lasts for 20 orbital cycles. The 15 GHz radio flux density during the second observation was ∼50 mJy. Based on simple arguments, they rejected the idea that QPOs are X-ray emitting blobs in a region of the accretion disk determined by the inner disk radius or the Roche Lobe radius. Other possibilities like an oscillating corona due to a magnetoacoustic wave propagation within the corona, an oscillation in the jet-base caused by the downward propagation of the relativistic shock from the jet, oscillation due to wind, etc., have been discussed but none of them have been confirmed as being the origin of mHz QPOs.

With the successful launch of the first Indian multi-wavelength astronomical mission AstroSat in 2015 (Agrawal 2006; Singh et al. 2014), a new window to investigate spectro-temporal properties of Cyg X-3 has been opened. Large Area X-ray proportional Counter (LAXPC), one of the payloads in *AstroSat*, consists of three independent units of proportional counters (LAXPC10, LAXPC20, LAXPC30) with the key feature of large effective area ∼4500 cm^2 at 30 keV (∼4–5 time higher than that of *RXTE*/PCA; Yadav et al. 2016a) and absolute time resolution of 10 μs. Details of the instrument and calibration can be found in Yadav et al. (2016b). LAXPC has already shown its capability to perform spectro-temporal variability study in micro-quasars like GRS 1915+105 (Yadav et al. 2016a) and Cyg X-1 (Misra et al. 2017). In this work, using several orbit data of Cyg X-3 during several epochs spanning over ∼400 days, we measure the binary orbital period of the system of 17253.56 ± 0.19 s and reconfirm the detection of ∼20 mHz QPO during FHXR state in Cyg X-3 using LAXPC on board *AstroSat*. An energy-dependent study shows soft-lag at 20 mHz (soft photons lag hard photons). We also perform spectral analysis during the rising and decay phase of the binary orbit to understand the connection between energy spectral and QPO properties as a function of binary phase. Section 2 provides observation and analysis procedures, while results are provided in Section 3. Discussions and conclusions are provided in Section 4.

2. Observations and Analysis

As a part of the payload verification (PV) phase calibration and guaranteed time (GT) observations, Cyg X-3 has been observed nine times by *AstroSat*/LAXPC covering many orbits (between 2015 October 24 and 2016 November 20). Details of LAXPC observations during each epoch are shown in Table 1. Spectral states provided in Table 1 are determined by qualitatively comparing the HID with Figure 3 from Koljonen et al. (2010) and by comparing the unfolded spectral shape (in units of keV^2 (photons s^{-1} cm^{-2} keV^{-1})) with Figure 4 from Koljonen et al. (2010). Details of spectral states and corresponding broadband energy spectral analysis will be provided in a subsequent paper. We check each orbit data for possible detection of QPOs and observations where QPOs are detected with at least 99% confidence are quoted in Table 1 with the number of detections. Observations on 2016 March 6 have QPO detection significance higher than 3σ and QPO fractional rms are highest among all detections. For this reason, we focus on the timing and spectral analysis of March data in this work. Remaining QPO detections have significance between 2.6 and 3σ. Using Equation (1), we calculate the binary phase of the light-curve intervals when QPOs are observed and provided them in the Table 1. We also note that the binary phase corresponding to the maximum count rate is 0.64 ± 0.01. Therefore, all seven QPOs are detected during the rising phase of the binary period during the FHXR state.

All observations are taken in Event Analysis (EA) mode with the absolute time resolution of 10 μs in the energy range of 3.0–80.0 keV. To check the source behavior, we also consider observations on 2015 November 27 and 2016 May 21, which are the two epochs closest to 2016 March observations. During these three epochs of *AstroSat* observations, we use the 15–50 keV *SWIFT*/BAT light curve to show hard flux behavior and the HID. The left panel of Figure 1 shows the one-day averaged BAT light curve, where three epochs of observations are shown by vertical gray lines. It may be noted that the hard X-ray count rate during 2015 November was ∼60% of that during 2016 March and May. This indicates that spectral hardening of the source occurred during the 2016 March–May observation compared to the 2015 November observation. This can be confirmed by the HID shown in the right panel of Figure 1. The hardness is defined as the ratio of the count rate in the energy range of 10–30 keV and 3–6 keV. Such definitions of hard and soft bands have been used previously on a few occasions (Fender et al. 2004; Dunn et al. 2010; Koljonen et al. 2011) and ensures mutually exclusive hard and soft bands in black hole X-ray binaries. The HID of 2015 November and 2016 March/May form parallel tracks in the HID and 2015 November HID is significantly softer (nearly by a factor of 2) than the HID observed on 2016 March and May.

Table 1
AstroSat/LAXPC Observation Details of Cyg X-3

Obs ID	Orbit Number	Date (dd-mm-yyyy)	All-orbit Combined Exposure (s)	Average Source Count Rate	Spectral State	QPO Observed ? (99% Confidence)	QPO Frequency (mHz)	QPO Occurrence	Binary Phase of QPO Intervals
58	377–386	2015 Oct 24	17364	1329 ± 17	FHXR	Yes	13.6 ± 0.7	1	0.338–0.466
98	683–697	2015 Nov 13	36475	1389 ± 25	FIM	No	⋯	⋯	⋯
180	896–904	2015 Nov 27	18239	1529 ± 33	FIM	No	⋯	⋯	⋯
360	2375–2393	2016 Mar 06	34203	1432 ± 24	FHXR	Yes	20.3 ± 1.1	3	0.459–0.604 0.176–0.367 0.226–0.347
466	3500–3508	2016 May 21	25885	1494 ± 25	FHXR	Yes	5.7 ± 1.7	1	0.452–0.612
522	4094–4099	2016 Jun 30	15172	1405 ± 22	FIM	No	⋯	⋯	⋯
526	4110–4114	2016 Jul 01	11016	1544 ± 28	FIM	No	⋯	⋯	⋯
594	4727–4737	2016 Aug 12	27183	2433 ± 39	FSXR	No	⋯	⋯	⋯
812	6204–6218	2016 Nov 20	33788	1418 ± 23	FHXR	Yes	5.9 ± 1.9	2	0.378–0.552 0.395–0.565

Note. During all LAXPC observations, the source showed three states: flaring hard X-ray state (FHXR), flaring intermediate state (FIM), and flaring soft X-ray state (FSXR).

Comparing with Koljonen et al. (2010), we find that 2016 March and May observations belong to the FHXR state, while the 2015 November observations belong to the flaring intermediate state (FIM). Such trends of parallel tracks have also been observed with *RXTE* (see Figure 1 of Koljonen et al. 2010). During the harder state and at the rising X-ray flux, 20 mHz QPOs are observed, the HID position of which is shown by red symbols in the Figure 1.

Based on good time intervals, when light curves from several consecutive orbits over one year are combined, covering many epochs as observed from Table 1, a strongly periodic modulation is observed. A careful observation of the light curve from different epochs shows both sinusoidal binary motion and its harmonics. Furthermore, a slower variation with the timescale of the order of ∼5 weeks is also observed. With this motivation, we assume that light curves from all epochs can be modeled with a function consisting of the addition of two sinusoids and their harmonics: one with faster variability of the order of the binary orbital period and the other with the slower variability of the order of a month timescale. The functional form of the model is

$$f(t) = a_0 + a_1 \sin(\omega_b t) + a_2 \cos(\omega_b t) + a_3 \sin(2\omega_b t) + a_4 \cos(2\omega_b t) + a_5 \sin(\omega_p t) + a_6 \cos(\omega_p t) + a_7 \sin(2\omega_p t) + a_8 \cos(2\omega_p t), \quad (1)$$

where ω_b and ω_p represent the orbital and precessional angular velocities and a_0 to a_8 are coefficients. Instead of addition, our fit with the function consists of the multiplication of two sinusoids and their harmonics, assuming that the slower and the faster varying components originated from the same physical process. The multiplicative function is not able to fit the observed profile. The reason for this is that the product function has a constant mean value when averaged over a shorter period, which is contrary to the observed increase in the mean value, at least during one observation (see the top left panel of Figure 2). This follows from the fact that if this signal is averaged over a shorter timescale (∼4.8 hr), then the slowly varying component (of the order of ∼5 weeks) will hardly change on that timescale, while the ∼4.8 hr factor will average to zero. Thus only the constant term will contribute to the average. The proposed model is fit to all nine observations of Cyg X-3 shown in the top left panel of Figure 2.

In order to determine the slowly varying component, ω_p, we have taken the entire light curve, spanning ∼400 days with gaps with a time bin of 60 s that will have a few thousand points and the fit involves nine coefficients in Equation (1) and fixed ω_p. The fit is done separately for each value of ω_p with the step size of 0.1 days between 32 and 42 days and for each step of ω_p, ω_b is varied in small steps (0.01 s) around its best-fit values so that we can get both simultaneously by looking for the minimum χ^2. The resulting fit is plotted in the central left panel of Figure 2, which shows χ^2/dof as a function period. The minimum of χ^2/dof obtained from variation of both periodicities is taken to be the best value giving the orbital and precession periodicities.

From the fitted parameters of the additive function given in Equation (1), we obtain the combined (combining measurements from three LAXPC units) orbital periodicity to be 17253.56 ± 0.19 s, which is consistent with the measured orbital period of the system and a slower variation of 35.8 ± 1.4 days, which is consistent with the periodicity of ∼34.1 days observed earlier from this source (Holt et al. 1976; Molteni et al. 1980) and it was explained using a free precession model of an elastic neutron star (Suto & Iso 1980). Table 2 provides orbital and precessional periodicities obtained from three LAXPC units individually and combined. The zero phase reference (57318.6545338 ± 0.0000578 MJD) corresponds to the first minima of the binary orbital period. The model-fitted curve and LAXPC20 count rate covering all epochs (provided in Table 1) spanning over nearly a year are shown in the top left panel of Figure 2. In the central left panel of Figure 2, the reduced χ^2 of the fitting of slowly varying component shows two apparent minima at ∼35.8 days and ∼38.2 days respectively. The reason for two periodicities is not clear; however, the minima at ∼35.8 days is lower than the minima at ∼38.2 days, more uniform and consistent with previous measurements. Therefore, in Table 2, we quote measurements at ∼35.8 days from three LAXPC units. It may be noted that we cannot rule out the possibility that the slow periodic variability is due to the window function convolution with the other period. However, putting random values for the

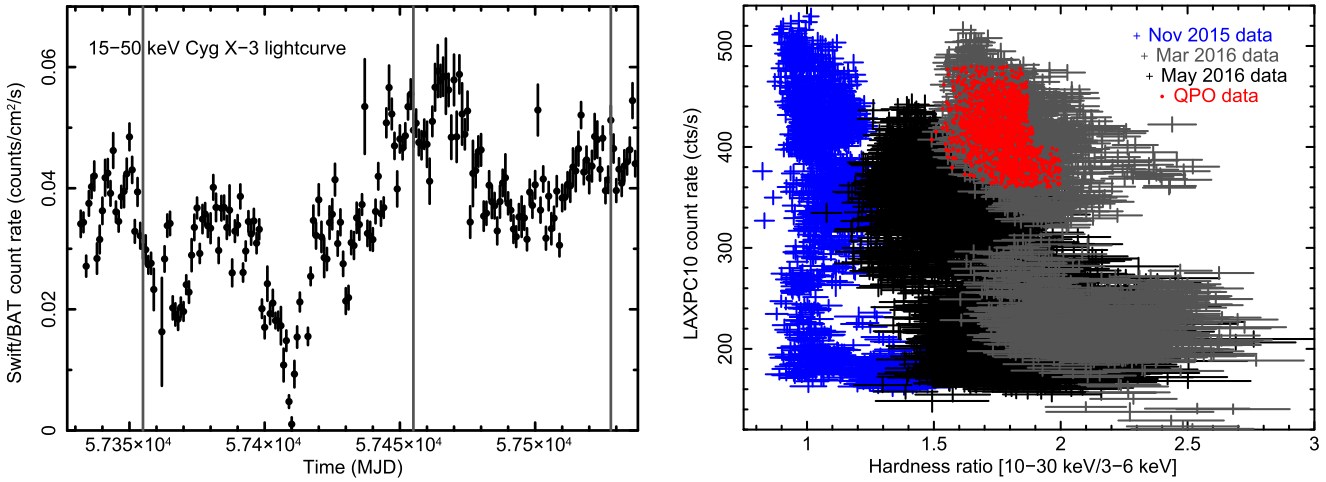

Figure 1. Left panel shows the 15–50 keV *SWIFT*/BAT light curve of Cyg X-3, where three vertical, gray lines mark the epoch of *AstroSat*/LAXPC observations on 2015 November, 2016 March, and 2016 May. The right panel shows the hardness intensity diagram (HID), where the 3–30 keV LAXPC10 count rate is shown as a function of the hardness ratio (ratio of the count rate between 10–30 keV and 3–6 keV). The HID of the 2015 November observation (shown as blue symbols) is clearly softer than the HID of 2016 March (shown as gray symbols). However, the HID during the 2016 May observation (shown as black symbols) occupy a region between 2015 November and 2016 March having a partial overlap with 2016 March HID. The HID position when mHz quasi-periodic oscillations are detected during 2016 March observation are shown by red symbols.

observed points or taking random combinations of nine sets of observations do not give any significant periodicity in this interval. However, in order to determine the long period reliably, we need many more data sets, so we can only drop the first few, or the last set, to check the effect of the window function. With just nine data sets, it is also difficult to rule out the presence of systematic variation in the long period. However, if the period is varying steadily then one would expect the χ^2/dof dip to be broadened and the width of dips can give some measure of variation. Since within ∼395 days of observations, about 10–11 periods are covered, we would expect a width of about 10%, which can include both dips in χ^2/dof versus period plot shown in the central left panel of Figure 2. The cadence of *Swift*/BAT light curve is not small enough to remove the effect of smaller period. Hence it is difficult to conclude systematic variations in the long-period oscillation from the BAT light curve.

For clarity, we show the zoomed version of the model along with `LAXPC20` count rate during three epochs of observations covering consecutive orbits of few tens of kiloseconds in top right and bottom panels of Figure 2.

Out of several orbits, we present PDS analysis of six LAXPC observations of Cyg X-3 during 2016 March as listed in Table 3. Each of them were obtained from a single orbit with effective exposure of ∼2–3 ks each. In three orbits, a QPO is detected significantly in the PDS, which is denoted by "Q1," "Q2," and "Q3," respectively, while observations from three orbits where no such QPO-like features are observed are denoted by "NQ1," "NQ2," and "NQ3" in Figure 3 and Table 3 respectively.

3. Timing Analysis and Results

A close inspection of Figure 3 and Table 1 reveal that QPOs are detected mostly in the observations that were obtained during the rising flux of the orbital phases. A 400 s section of the light curve of three observations—"Q1," "Q2," and "Q3" is shown in the top panels of Figure 4 respectively. Light curves from all three LAXPC units are combined and background subtracted. A bin size of 5 s is used. A quasi-periodicity in low-amplitude flares of the order of ∼40–60 s can be observed from all three light curves in Figure 4. Top right panel shows ∼50 s flares on the top of a large flare of the order of ∼300 s.

3.1. LAXPC Rising-phase PDS Analysis

PDS are derived from "Q1," "Q2," and "Q3" light curves in the energy range of 3.0–80.0 keV, 3.0–15.0 keV and 15.0–80.0 keV and shown in the second, third and fourth rows of panels in the Figure 4. Combining light curves from three LAXPC units in three energy bands, PDS are derived. All PDS are rms-normalized and deadtime-corrected Poisson-noise subtracted. Details of deadtime-corrected Poisson-noise estimations are discussed in Yadav et al. (2016a). PDS are plotted in the frequency range of 1–100 mHz using suitable geometric rebinning for the clarity of any feature. In Figure 4, for all three PDS in 3.0–15.0 keV (all panels in the third row) and 15.0–80.0 keV (bottom panels) energy bands, a QPO-like feature is observed at ∼20 mHz. To determine strength and significances of such features, the PDS continua are fitted with a broken power law, while the QPO-like feature is fitted with Lorentzian. QPO frequencies as obtained from fitted Lorentzian centers are quoted in Table 3.

The significances of such QPO-like features are computed by dividing the area under the Lorentzian at the QPO position with the 1σ negative error of model-estimated area. Detection significances of QPOs in "Q1," "Q2," and "Q3" are quoted in Table 3. We calculate the confidence level of detected QPOs following the recipe for testing the significance of peaks in the periodogram of red noise data provided by Vaughan (2005). If the red noise can be fitted by a power-law-like continuum, then low significance peaks can be rejected accurately using this recipe. We find that the peak X-ray power in "Q1," "Q2," and "Q3" PDS at the QPO frequency is higher than the power predicted at least at the 99.0% confidence level. Using the fitted Lorentzian parameter, fractional rms is estimated and then they are corrected for the background by multiplying by the factor R/S; where R is the raw, observed count rate and S is the background-subtracted source count rate. 3.0–80.0 keV fractional rms of "Q1," "Q2," and "Q3" are quoted in Table 3.

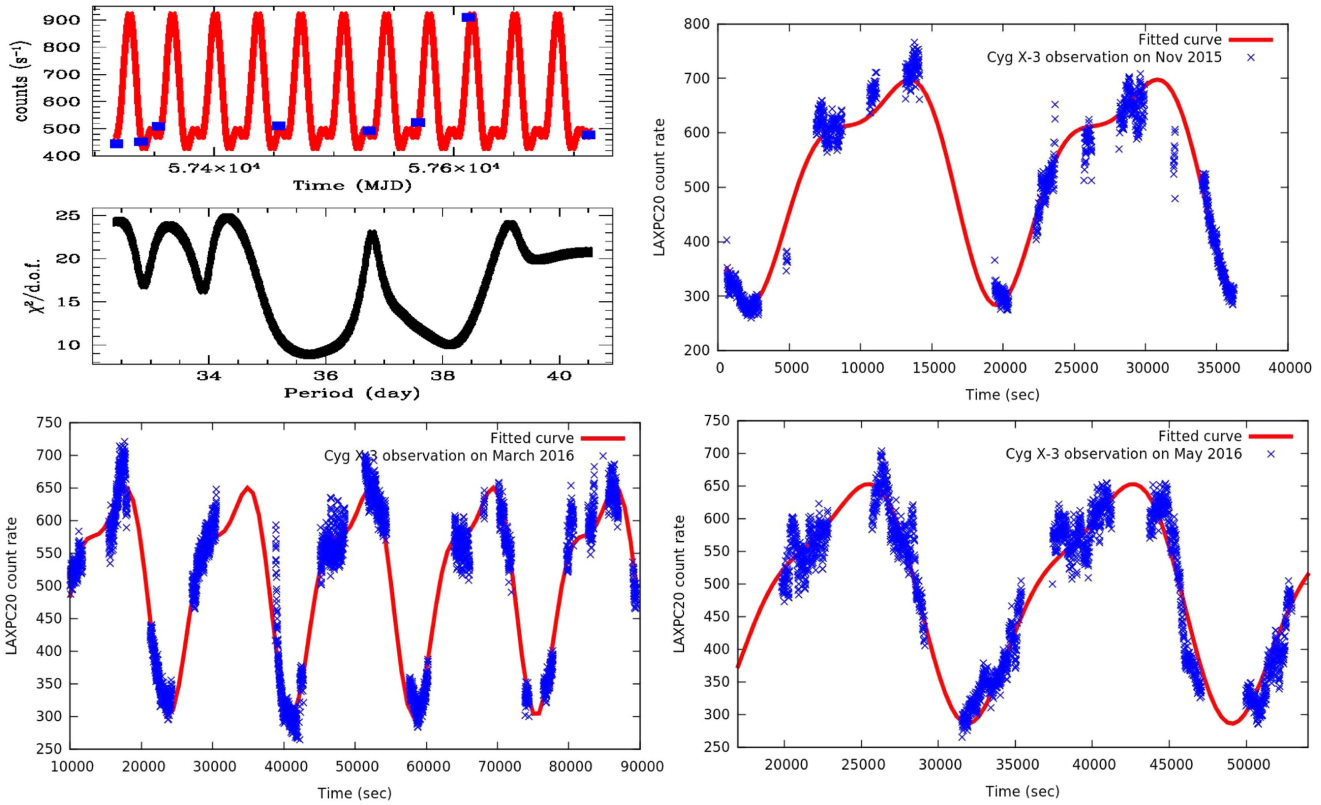

Figure 2. Upper figure in the top left panel shows the background-subtracted LAXPC20 count rate (in blue squares) observed over many epochs covering one year of *AstroSat* observations. The variations can be modeled (in red) well with two sinusoids and its harmonics: one with a binary orbital period of ∼4.8 hr and another with a precessional orbital period of ∼35 days. Centeral left panel shows the reduced χ^2 (χ^2/dof) of the sinusoidal fitting of the slowly varying component as a function of days. Two minima at ∼35.8 days and ∼38 days are obtained from the fitting. For clarity, the fitted sinusoidal model and its harmonic (in red) are zoomed along with the background-subtracted 3–80 keV LAXPC20 light curve of Cyg X-3 (in blue) from consecutive orbits of several tens of kiloseconds and shown in the top right and bottom panels during 2015 November, 2016 March, and 2016 May observations respectively.

Table 2
Orbital Period Measurements of Cyg X-3 Using Different Epochs of LAXPC Observations

LAXPC Units	Average Orbital Period (s)	Precessional Period (days)
LAXPC10	17253.55 ± 0.18	35.7 ± 1.4
LAXPC20	17253.49 ± 0.21	35.7 ± 1.3
LAXPC30	17253.68 ± 0.11	36.0 ± 1.5
All units combined	17253.56 ± 0.19	35.8 ± 1.4
Zero phase reference	57318.6545338	±0.0000578 (MJD)

3.1.1. RXTE/PCA PDS Analysis

As pointed out by Koljonen et al. (2011), during the FHXR state, an ∼22 mHz QPO from Cyg X-3 is detected at the significance level higher than 99% with the *RXTE*/PCA observation on 2009 August 09. We reanalyze the same observation and extract Poisson-noise subtracted PDS in three different energy bands: 2–10 keV, 10–14 keV, and 14–60 keV. The choice of bands are restricted by the PCA default channel binning. Top left panel of Figure 5 shows the PDS in 2–10 keV, where a strong QPO-like feature is observed at ∼22 mHz. We fit the PDS with a combination of power law and Lorentzian and compute the significance of the QPO using the method described above. The fit returns the QPO at 22.8 ± 0.5 mHz with the QPO significance of 3.3σ. Interestingly, no Lorentzian are required to improve the fit significantly at the position of the QPO frequency in the PDS extracted at 10–14 keV (top right panel of Figure 5) and 14–60 keV (bottom left panel of Figure 5). QPO significance at ∼22 mHz in 10–14 keV and 14–60 keV are $<3\sigma$ and $<2\sigma$ respectively. This is in sharp contrast with the *AstroSat*/LAXPC observation of ∼21 mHz at higher energy. In the 15–80 keV energy range, QPOs are detected at the significance of $>3\sigma$. The only reason of the detection of QPO at high energy with LAXPC and not with PCA is the efficiency of LAXPC, which is higher by a few factors than PCA above 20 keV (at 20 keV, the effective area of *RXTE*/PCA is ∼1500 cm^2 (Jahoda et al. 2006), while the effective area of *AstroSat*/LAXPC is ∼6000 cm^2 (Antia et al. 2017)). The section of the *RXTE*/PCA light curve that shows mHz QPO is plotted in gray in the bottom right panel of Figure 5. The binary phase of the time interval when *RXTE*/PCA QPO is observed is calculated in the range of 0.231–0.335 using Equation (1). This phase interval also belongs to the rising phase of the binary motion and the range partially overlaps with a couple of QPO detections with LAXPC (see Table 1).

3.2. LAXPC Decay Phase PDS Analysis

A ∼400 s section of light curve of three observations —"NQ1," "NQ2," and "NQ3"—are shown in the top panels of Figure 6 respectively. Similar procedures are used to extract light curves. None of the light curves show low-amplitude, quasi-periodic ∼40–60 s flare-like structures, although large flares of the order of ∼300 s are observed in the "NQ2" light

Table 3
Details of QPO Properties Observed from Cyg X-3 During 2016 March Observation

ID no.	Orbit Number	Date (dd-mm-yyyy)	Effective exposure (s)	Background-subtracted Source Count Rate	QPO Frequency (mHz)	QPO Fractional rms (%) (3.0–80.0 keV)	QPO Detection Significance (σ)
Q1	2379	2016 Mar 06	2523.0	1943 ± 34	17.9 ± 0.5	0.97 ± 0.05	∼3.7
Q2	2381	2016 Mar 06	3321.0	1648 ± 25	23.2 ± 0.9	1.47 ± 0.06	∼3.5
Q3	2386B	2016 Mar 07	3380.0	1715 ± 28	21.3 ± 0.4	1.23 ± 0.05	∼4.2
NQ1	2380	2016 Mar 06	2953.0	962 ± 22	⋯	⩽0.35[a]	⋯
NQ2	2386A	2016 Mar 07	2831.0	848 ± 19	⋯	⩽0.43[a]	⋯
NQ3	2387	2016 Mar 07	2545.0	877 ± 19	⋯	⩽0.39[a]	⋯

Note.
[a] The 3σ upper limit of the fractional rms (per cents) measured from fitted PDS continuum (1–200 mHz) when QPO is detected.

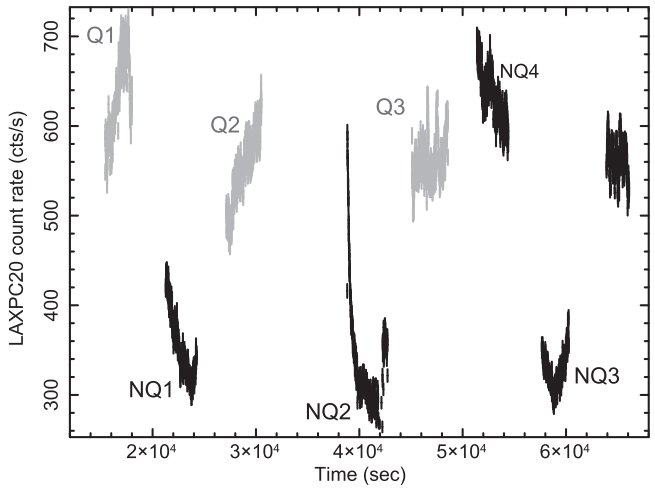

Figure 3. LAXPC20 light curve of Cyg X-3 in the energy range of 3.0–80.0 keV covering many *AstroSat* orbits continuously. The ∼20 mHz QPOs are detected during the rising phase of binary orbits (shown in gray) with at least 3σ significances in three observations marked with "Q1," "Q2," and "Q3." For clarity, observations where no QPOs are observed up to 2σ significance and analyzed here are marked as "NQ1," "NQ2," "NQ3," and "NQ4."

curve, similar to what is observed from the "Q3" light curve. Following previous methods, we derive rms-normalized, deadtime-corrected Poisson-noise subtracted PDS from "NQ1," "NQ2," and "NQ3" light curves in 3.0–80.0 keV energy range. Bottom panels in Figure 6 show PDS from "NQ1," "NQ2," and "NQ3," respectively, in the frequency range from 1 to 100 mHz. Although the strong noise component is observed below ∼15 mHz, which rises at lower frequencies, no QPO-like features are observed from all PDS at ∼20 mHz. In order to show that the low source count rate during "NQ1," "NQ2," and "NQ3" (from top panels of Figure 6) and nondetection of QPOs are not correlated, we select a high count rate observation (comparable to that when QPO is detected) during the decay phase of the binary motion and marked by "NQ4" in the Figure 3. The 5 s binned light curve with the exposure of ∼3 ks is shown in the top left panel of Figure 7 and the corresponding power density spectrum is shown in the top right panel. No QPO detected in the PDS implies that QPO detection does not depend on source count rate in Cyg X-3 and QPOs are observed mostly during the rising phase of the binary orbital motion. In order to show whether mHz QPOs are spectral state dependent, we consider the rising phase light curve of the FSXR, which is shown in the bottom left panel of Figure 7 and its corresponding PDS in the bottom right panel. The PDS shows no signature of mHz oscillations, which probably imply that ∼20 mHz QPO is more common in the FHXR state.

To compare PDS with and without QPOs, we plotted them together in the top left panel of Figure 8. It clearly shows no QPO during the light curve of the decay orbital phase, while a strong QPO-like feature is present in the light curve during the rising orbital phase. A PDS during "Q3" fitted with a combination of broken power law and Lorentzians is shown in the top right panel of Figure 8, where different model components and residual of the fit are also shown. 3.0–80.0 keV dynamic power spectra (DPS) of light curve with ("Q3") and without ("NQ1") QPO are shown in the bottom panels of Figure 8. DPS are extracted using `fgabor` tool in `FTools v 6.18`, which performs a Gabor transformation on a light curve and return the normalized power as a function of time and frequency. In the frequency range of 10–40 mHz, the DPS of "Q3" in Figure 8 shows strong excess around 20 mHz ($(\mathrm{rms/mean})^2\,\mathrm{Hz}^{-1} > 0.0085$), although it is quasi-continuous and the power varies with time. Such strong excess is absent from the DPS of "NQ3," where $(\mathrm{rms/mean})^2\,\mathrm{Hz}^{-1} < 0.0033$ with 3σ significance.

3.3. Time-lag and rms Spectra

Event mode data from LAXPC distributed over 1024 channels allows us to compute time delay between photons at different energies. Time-lag are calculated at ∼21.3 Hz QPO frequency during the "Q3" observation, in which the QPO detection significance is highest. The 10–14 keV energy band is selected as the reference band since the QPO fractional rms at this energy range is moderately high. Details of the time-lag calculation and its error estimations are provided in Nowak et al. (1999), time-lag spectra are shown in the top panel of Figure 9. At higher energy (>7 keV), a significant soft lag, where soft X-ray photons lag hard X-ray photons, is observed. Background-corrected fractional rms of the QPO observed from both *RXTE*/PCA and *AstroSat*/LAXPC are calculated at different energy bands and shown using gray and black symbols, respectively, in the bottom panel of Figure 9. Fractional rms is found to increase with photon energy from both instruments. With *AstroSat*/LAXPC observations, energy-dependent lag and rms calculations are restricted to 30 keV due to a poor signal-to-noise ratio at higher energies.

4. Spectral Analysis and Results

To find out the change in spectral properties while the source moves from the rising orbital phase to the decay orbital phase and to connect such changes with the appearance and disappearance of QPOs at the rising and decay orbital phase,

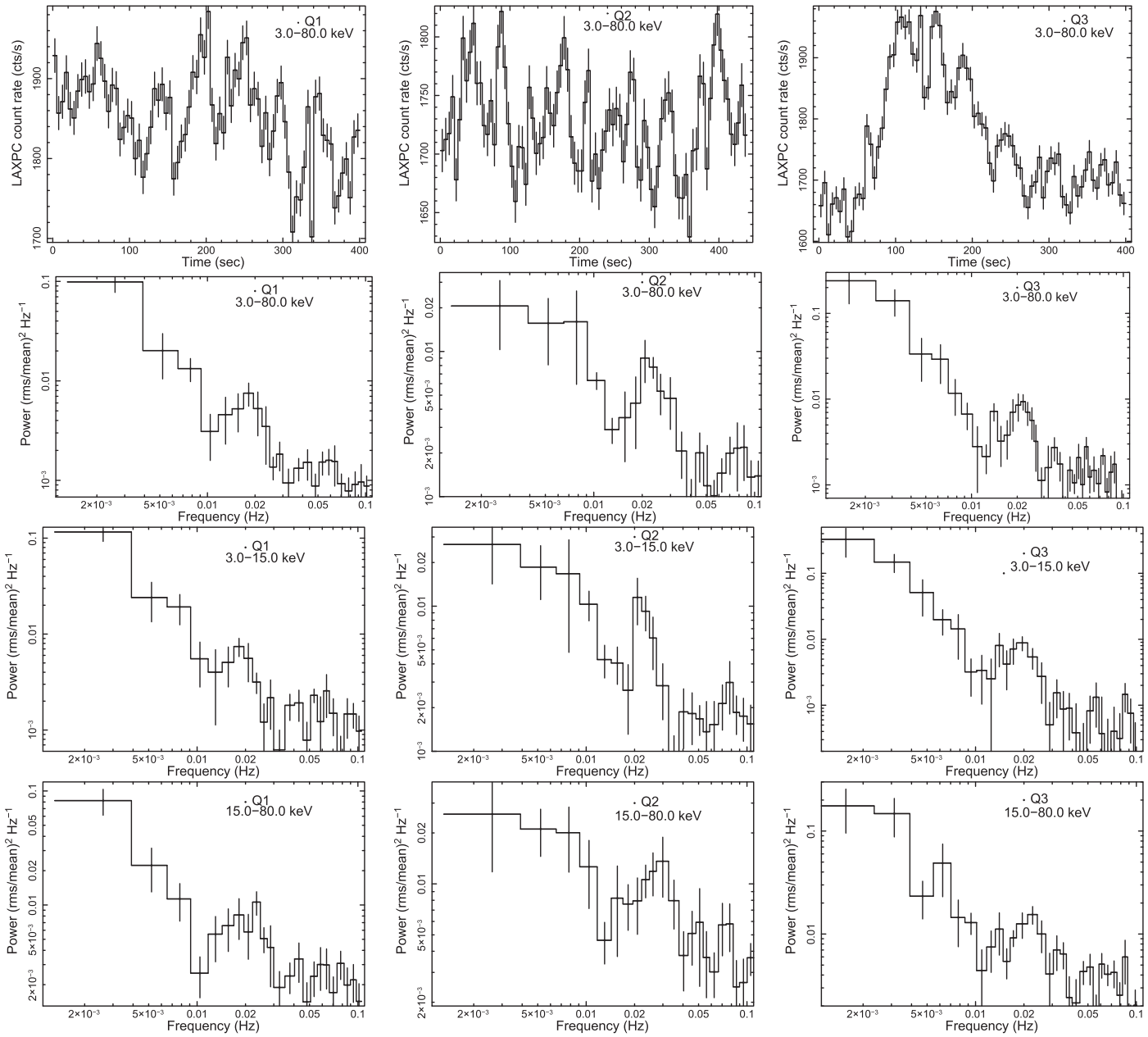

Figure 4. Top panels in three columns show ∼400 s section of light curve from each of the observations (Q1, Q2, and Q3), where ∼20 mHz QPOs are detected. For better visibility of ∼50 s (1/20 mHz) oscillations, 400 s segments are used. Light curves are binned to 5 s. Second rows of panels show 3.0–80.0 keV Poisson-noise subtracted power density spectra from Q1, Q2, and Q3 (left to right). Third and fourth rows of panels show PDS in the the energy range of 3.0–15.0 keV and 15.0–80.0 keV respectively. All PDS are Poisson-noise subtracted and derived from observations combining all three LAXPC units. In three energy ranges (3.0–15.0 keV, 15.0–80.0 keV, and 3.0–80.0 keV) ∼20 mHz QPOs are observed from all PDS with variable strength.

we perform average energy spectral analysis in the energy range of 4.0–60.0 keV of "Q1" observation, which resides at the rising phase and "NQ1," which resides at the decay phase, immediately after "Q1" (see Figure 3). The response function for each of the LAXPC units is computed using GEANT4 simulations (Yadav et al. 2016b; Antia et al. 2017) and the background for each of the units is modeled using blank sky observation at different position of the satellite in its orbit (Antia et al. 2017). A 4% uncertainty on the model background count rate is added and 1.5% model systematic error is introduced. The spectral fitting is performed using the XSPEC v 12.9.0n fitting package.

It has already been noticed several times that an absorbed thermal Comptonization is the predominant component in the energy spectra (Vilhu et al. 2003; Koljonen et al. 2013). To fit energy spectra during "Q1" and "NQ1," we use the same best-fit model as described in Koljonen et al. (2013) except the BELM thermal/nonthermal hybrid Comptonization model. Koljonen et al. (2013) used highly sensitive, broadband spectra in the energy range of 1–100 keV from multiple instruments. Therefore, the complex, self-consistent, hybrid model like BELM, which in addition to the thermal/nonthermal Comptonization, self-consistently considers the disk spectrum as the origin of soft seed photons as well as compute reflection fraction from the disk. It is suitable for describing broadband, high quality spectra. However, our spectral analysis is restricted to 4–60 keV and the spectra are not sensitive enough to probe hybrid corona. Therefore, we find that instead of a complex model, like BELM, a

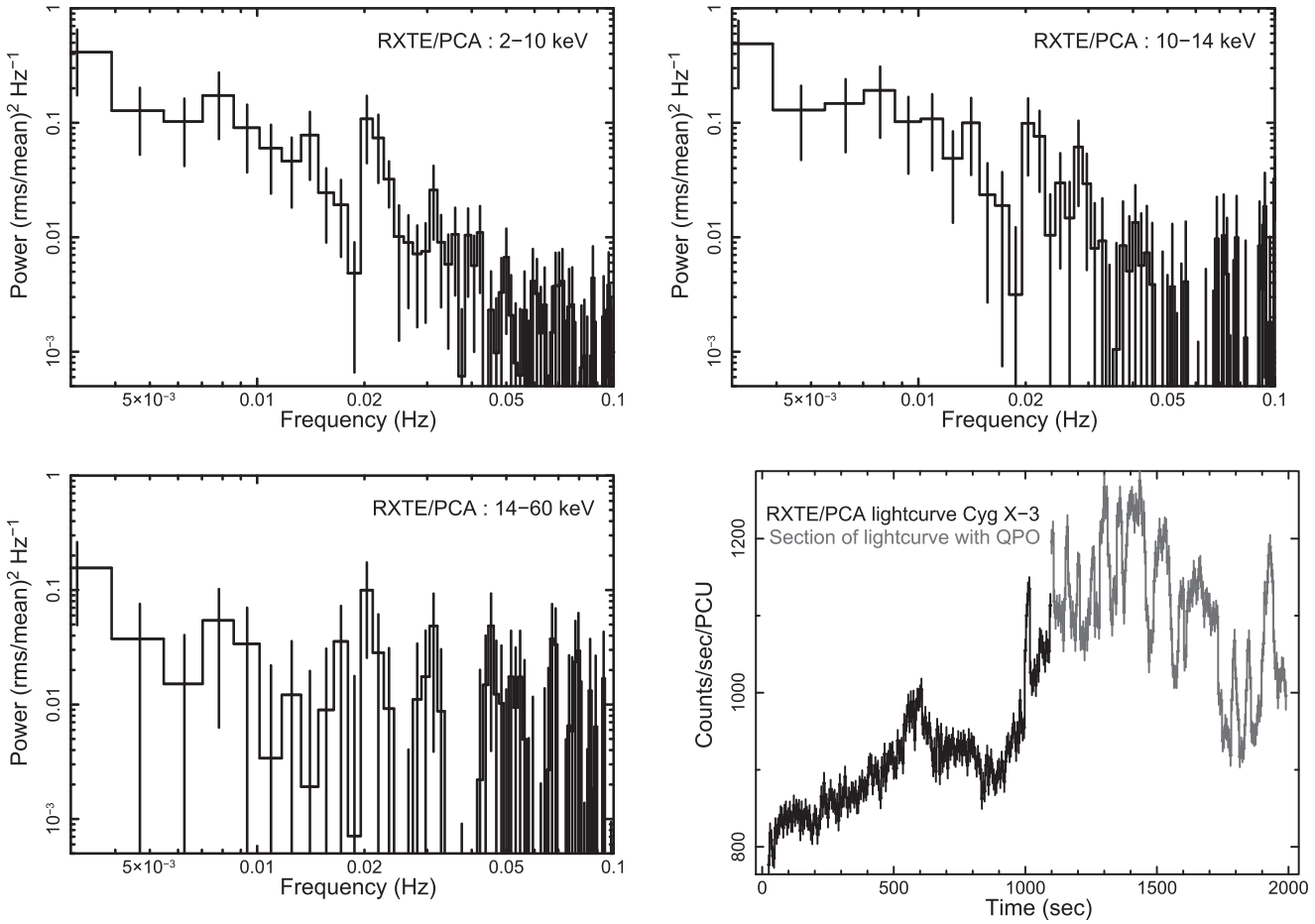

Figure 5. *RXTE*/PCA observation of Cyg X-3 on 2009 August 09: top left panel shows 2–10 keV Poisson-noise subtracted power density spectra (PDS), where ∼21.8 mHz quasi-periodic oscillation (QPO) is observed at the significance of $>3\sigma$. The PDS in the 10–14 keV and 14–60 keV energy ranges are shown in the top right and bottom left panels, where no QPO at ∼21.8 mHz is detected up to 3σ. The 2–60 keV light curve is shown in the bottom right panel, where the section of light curve that shows ∼21.8 mHz QPO is marked in gray. The binary phase of the *RXTE*/PCA light curve when the QPO is observed is 0.231–0.335 as calculated using Equation (1).

simpler model consisting of a disk blackbody (`diskbb` in `xspec`), a thermal Comptonization (`nthcomp` in `xspec`), and a disk reflection model `reflionx` (Ross & Fabian 2005) can describe the LAXPC spectra well in 4–60 keV. We replace the absorption model `phabs` with `tbabs`. With the addition of a narrow Gaussian emission line at 6.97 keV and two edges at ∼5.8 keV and ∼9.6 keV, the spectral fitting improves significantly with $\chi^2/\mathrm{dof} = 215/229$ for the rising phase spectrum and 233/229 for the decay phase spectrum. Our best-fit model is `pcfabs × tbabs × edge(1) × edge(2) × [diskbb + nthcomp + reflionx + bremss + Gauss]`. Fitted rising and decay phase spectra along with model components and residuals are shown in the top and middle panels of Figure 10.

During both the rising and decay phase spectral fitting, we fix the value of `tbabs` to the line-of-sight absorption column density $2.0 \times 10^{22}\,\mathrm{cm}^{-2}$, which is consistent with earlier works (Dickey & Lockman 1990; Predehl & Schmitt 1995). Since the normalization of the disk blackbody model is unconstrained, we fixed it at 1350, assuming the disk resides at a distance of $6r_g$ for a black hole mass of $6M_\odot$ and the inclination angle of 70°. During the rising and decay phase, the disk temperature is found to be 0.74 ± 0.14 and 0.47 ± 0.22 keV respectively. While the Comptonizing plasma temperature predicted by the `nthcomp` model is similar (5.8 ± 0.1 keV), the photon power-law indices during rising and decay phases are 2.01 ± 0.11 and <1.65 respectively. Therefore, a hint of change in spectral shape is observed from the fitted parameter. This is also supported by the fact that the ratio spectrum, which is the ratio between the rising and decay spectral count rate as a function of photon energy, deviates significantly from 1 below 50 keV, which is shown in the bottom panel of Figure 10. While moving from the rising phase spectral fitting to the decay phase, the partial covering fraction decreases from 0.94 ± 0.02 to 0.72 ± 0.04, the normalization due the Comptonization model decreases by a factor of ∼3 and the normalization due the thermal Bremstrahlung model decreases from 5.85 ± 1.14 to 2.12 ± 0.99. Changes in spectral parameters with phase are highly consistent with that observed from the phase circle diagram of Koljonen et al. (2013) and the phase-dependent wind accretion geometry of the system presented in Figure 14 of Koljonen et al. (2013).

5. Discussion and Conclusions

In this work, using *AstroSat*/LAXPC observations of Cyg X-3 covering nearly one year, we determined the binary orbital period of the system to be 17253.56 ± 0.19 s and a longer orbital period of the order of ∼35.8 days, which may be consistent with the precessional motion of the jet. However, two minima in χ^2/dof plots are obtained at ∼35.8 days and

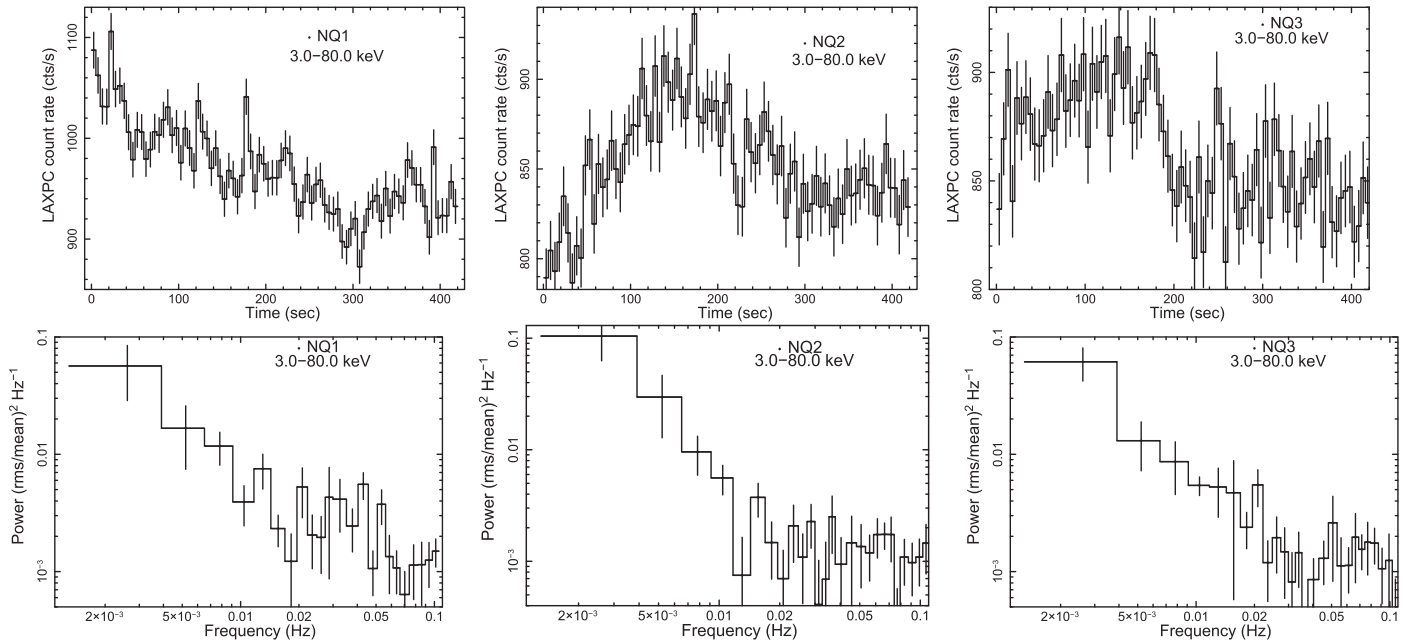

Figure 6. Top panels show an ∼400 s section of light curve from each of observations (NQ1, NQ2, and NQ3), where no QPOs are detected between 1 and 100 mHz. For comparison with Figure 4, 400 s segments are used. Light curves are binned to 5 s. All light curves are background-subtracted and combined using three LAXPC units. The second row of panels shows 3.0–80.0 keV Poisson-noise subtracted power density spectra from NQ1, NQ2, and NQ3 observations (left to right), where no obvious features are present.

∼38.2 days (top left panel of Figure 2), which is possibly caused by the fitting of the light curve from different observations, where one of them shows a very high average count rate (by a factor of ∼2). The fitting could be improved in the future using more observations with high average count rate and the measurement degeneracy between two values of the slow periodic components could be resolved.

It may be noted that previously using *EXOSAT* data, spanning over two years (1983–1985), the orbital period was measured to be 17252.52 ± 0.05 s using cubic ephemeris fit (van der Klis & Bonnet-Bidaud 1989). Later, combining *ASCA*, *ROSAT*, *BeppoSAX*, and *RXTE* observations, covering nearly seven years (1994–2001), Singh et al. (2002) determined the orbital period of 17252.95 ± 0.04 s and the rate of change in orbital period to be $7.7 \pm 1.5 \times 10^{-10}$ s s^{-1}. Compared to the orbital period measurement by Singh et al. (2002), the current binary period, measured from the present work is longer by ∼0.60 s. In order to justify the increased orbital period, we calculated the predicted orbital period by assuming their orbital period derivative measurement is robust. Considering its upper limit, the predicted current orbital period (2015–2016) should be 17253.43 ± 0.11 s with the same binary orbital decay rate. This is consistent with *AstroSat*/LAXPC measurements of binary orbital period using data from epochs spanning over nearly one year. If this is true, then these results suggest that the binary system continues to slow down the binary orbital motion at a nearly similar rate.

During the flaring hard state, we detect the mHz QPOs and energy-dependent time lag and rms spectra from three different observations of Cyg X-3 all of which were taken using *AstroSat*/LAXPC in 3.0–80.0 keV during the rising part of the orbital phase. Three QPOs during 2016 March, in the frequency range of 17–23 mHz are visible in 3.0–15.0 keV as well as 15.0–80.0 keV energy bands and such quasi-periodic variability of the order of ∼40–60 s is also observed in the light curve obtained from combining three LAXPC units. Noticeably, during the decay of the orbital phase, no QPOs have been observed at any frequency up to 100 mHz from three different observations. This implies that the QPO is quasi-persistent and mostly observed during the rising part of the light curve rather than the decay part. It may be noted that the detection of such quasi-periodic features in the light curve is independent of the count rate statistics. Figure 3 clearly shows that no QPOs are detected during the decay phase of the light curve even if it has a higher count rate than the rising phase where QPO is detected. Such a phase-dependent trend of the occurrence of QPOs is also consistent with that observed from *RXTE*/PCA (see the bottom right panel of Figure 5).

It may be noted that QPOs at ∼21 mHz were also observed by Koljonen et al. (2011) during the FHXR state. Dominant Comptonization, lack of disk component in the spectra from our analysis indicates that the ∼20 mHz QPO detection occurs during the hard state. This can be confirmed by the 15.0–50.0 keV *Swift*/BAT light curve that shows the AstroSat/LAXPC observation was taken during the flaring hard state. Therefore, a 20 mHz QPO detection is consistent with earlier measurements. Not only that, in the context of phase, Koljonen et al. (2011) observed that 20 mHz QPOs occurred between phases 0.2 and 0.7. Interestingly, the QPOs discussed in van der Klis & Jansen (1985) also appear exclusively in the phase interval 0.0–0.75 that corresponds to the rising part of the phase-folded X-ray light curve (Vilhu et al. 2003). All QPOs reported here are detected in the rising phase in the orbit-modulated light curve.

5.1. On the Origin of mHz QPOs in Cyg X-3

The origin of mHz QPOs is not well understood. Previously, mHz QPOs were promptly observed from two black hole X-ray binaries: GRS 1915+105 (Belloni et al. 2000) and IGR J17091-3624 (Altamirano et al. 2011) and once from H 1743-322 (Altamirano & Strohmayer 2012). To explain the origin of

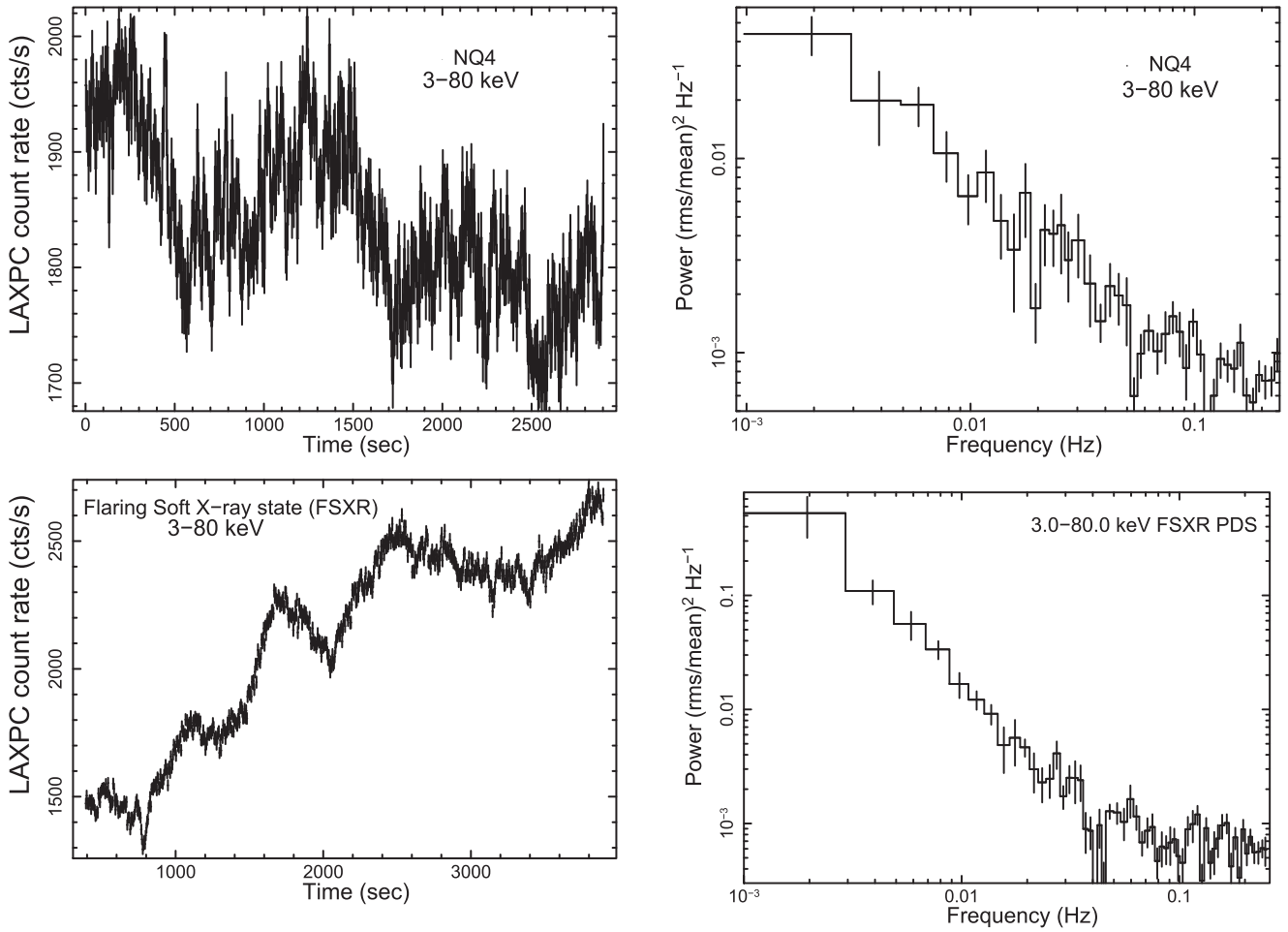

Figure 7. Top left and right panels show the 5.0 s binned light curve of Cyg X-3 during the decaying phase of the binary orbital motion (shown by "NQ4" in Figure 3) and the corresponding power density spectrum respectively. Despite of the high count rate and sufficient exposure, no QPO-like feature is visible in the Poisson-noise subtracted and background-corrected PDS. This implies that the detection of QPO is exclusive to the rising phase of binary orbital motion. Bottom left and right panels show the 5.0 s binned light curve of Cyg X-3 during the rising binary phase of the flaring soft X-ray state (FSXR) and the corresponding power density spectrum respectively. Despite of the rising phase in FSXR state and sufficient exposure, no QPO-like feature is visible in the Poisson-noise-subtracted and background-corrected PDS. This implies the 20 mHz QPO may be state dependent.

mHz oscillations from GRS 1915+105 (also known as heartbeat oscillations), a scenario like inward fluctuation propagation from a large distance in the accretion disk, was invoked (Neilsen et al. 2011), and to produce such an oscillation, a major contribution of the disk is suggested. Between two sources, mHz QPOs are observed during the soft state in IGR J17091-3624 (Pahari et al. 2014), while an 11 mHz QPO is observed during the hard/hard to hard/intermediate state transition in the low-mass X-ray binary (LMXB) H 1743-322 (Altamirano & Strohmayer 2012). During the soft state, disk blackbody flux dominates the spectra while during the hard state, nonthermal power-law-like emission dominates (Remillard & McClintock 2006). Therefore, it is natural that the disk association with the origin of mHz QPOs would be important to consider. Unlike LMXBs, the scenario in Cyg X-3 is quite different as mHz QPOs are observed in this system, which is dominated by the wind-fed accretion from the WR companion. The spectral analysis confirms the hard state nature when the QPO is detected and the disk component is not very strong. From our analysis, we observe that QPOs disappear during the falling part of the orbital phase and reappear during the rising orbital phase. Not only that, Table 1 shows that mHz QPOs are detected seven times only during the FHXR state. Therefore, broadband, orbital phase-resolved energy spectra during the FHXR state may be useful to investigate the origin of mHz QPOs. However, we may note that, apart from the FHXR state, Koljonen et al. (2011) detected mHz QPOs also during the FSXR state using the *RXTE* archival data between 1997 and 2011 (∼700 ks). Hence it is possible that we detect QPOs only during the FHXR state because of the small sample size (∼219 ks; adding all exposures in Table 1). Nevertheless, our results show that chances of detecting mHz oscillations are maximum during the FHXR state. Therefore, the origin of QPOs may have connections with the spectral state. During the FHXR state, variable radio emission is observed (Koljonen et al. 2010) from minor flaring (∼300 mJy) to major flaring (∼1 Jy). We, therefore, cannot rule out the possible role of the radio jet contributing to the origin of QPOs. An in-depth analysis in this direction is beyond the scope of the present work.

Comparing results from the energy spectral analysis in 4–60 keV during the rising and decay orbital phase with the phase circle diagram and the top panel of Figure 6 from Koljonen et al. (2013), we find that, the the orbital phase when QPOs are detected from *AstroSat*/LAXPC corresponds to the binary phase in the range of 0.18–0.61 (see Table 1), while no

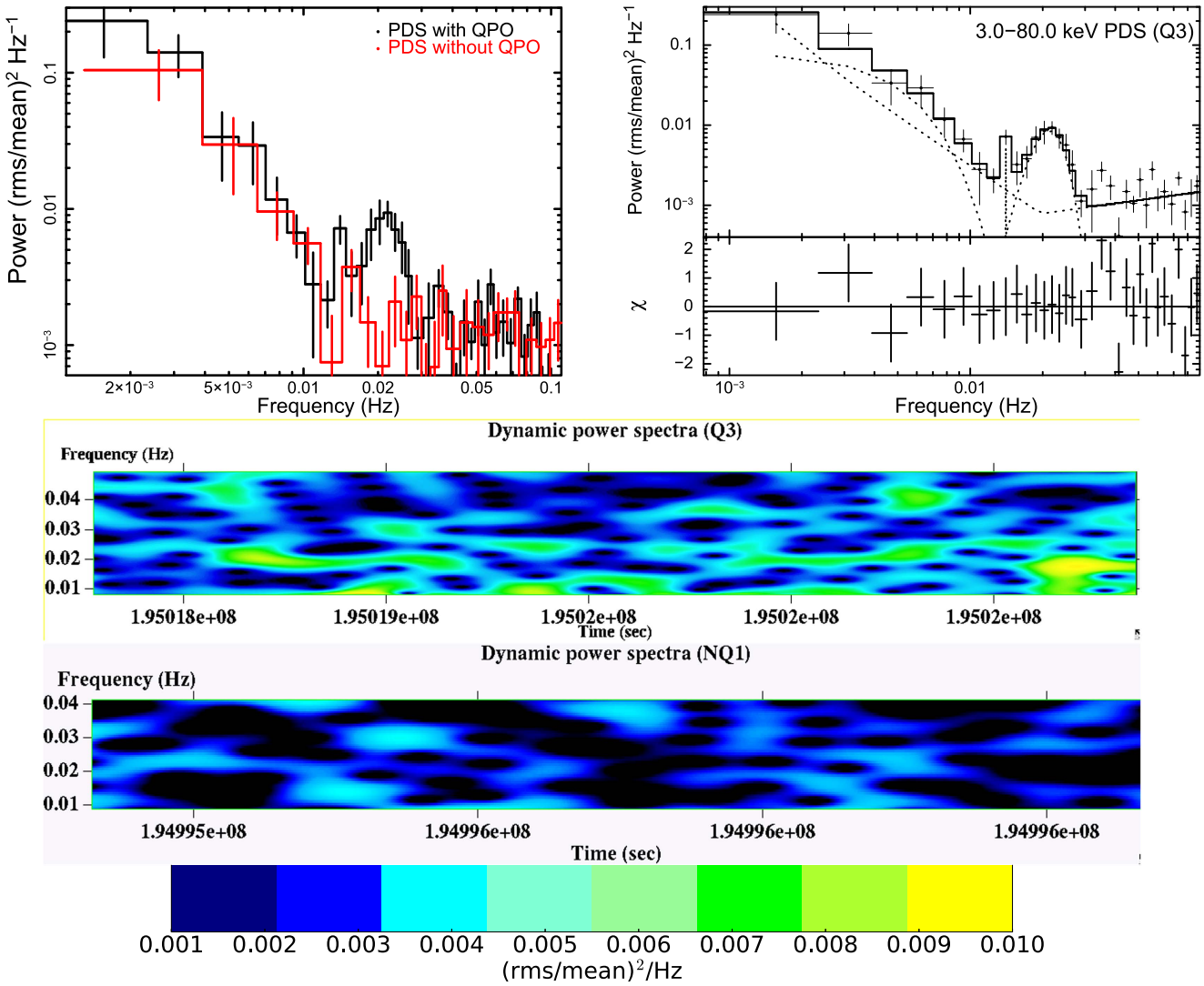

Figure 8. Top left panel shows two Poisson-noise subtracted power density spectra (PDS) plotted together when QPO is detected (black) and no QPO is detected (red). Top right panel shows PDS during the Q3 observation in the energy range of 3.0–80.0 keV fitted with a combination of a broken power law and two Lorentzians along with its residual. The middle panel shows dynamic power spectra (DPS) from the light curve when QPO is detected (Q3) and the bottom panel shows DPS from the light curve when no QPO is detected. Clearly a semi-persistent QPO is detected in the middle panel at ∼20 mHz, which is absent from the bottom panel.

QPO is detected in the remaining phase intervals, which mostly correspond to the decay of binary phase. As observed from the energy spectral analysis presented here and the phase circle diagram presented in Koljonen et al. (2013), major differences between fitted spectral parameters obtained from the rising and decay orbital phases are that (1) the covering fraction sharply decreases from 92% to 94% during the rising phase to 70%–73% during the decay phase. A decrease in a covering fraction of ∼20% implies that the source during the decay phase moves out of the region that is dominated by the wind accretion (see Figure 14 from Koljonen et al. 2013). Therefore, the shortage of the supply of the accreting material during the decay phase of the orbital motion may cause QPO to disappear below the detection limit. Another indication comes from the increase in the normalization of the Comptonization and thermal Bremsstrahlung emission models by a factor of ∼3 and ∼2, respectively, while moving from the decay to the rising phase spectra. During the rising phase, wind accretion is strongest as observed in the Figure 14 from Koljonen et al. (2013) and importantly, the optical depth is highest among all spectral states (>2.9; Koljonen et al. 2010). Therefore, the formation of a large scattering medium is inevitable. By modeling the effect of Compton scattering on timing properties in Cyg X-3, Zdziarski et al. (2010) estimated the size of the scattering cloud R_s as

$$R_s \simeq 1.5 \times 10^{10}\,\mathrm{cm}/\tau_s \times (f_c/1\,\mathrm{Hz}), \quad (2)$$

where τ_s is the optical depth of the scattering medium and f_c is the cut-off frequency. Considering the strongest QPO detection using LAXPC at ∼20 mHz (assuming no power in the PDS above this frequency) and the typical optical depth of ∼7 (Zdziarski et al. 2010) during the FHXR state, we estimated the size of the scattering cloud to be $\sim 1.6 \times 10^{11}$ cm, which is smaller/comparable to the size of the binary separation of 3.0×10^{11} cm (Szostek & Zdziarski 2008) in Cyg X-3. Therefore, the size of the scattering medium is appropriate enough to sustain the 20 mHz oscillations. Multiple QPOs detected during this phase may originate from the accretion of the oscillating clumpy stellar wind from the companion (Szostek & Zdziarski 2008) and the strength of QPOs may

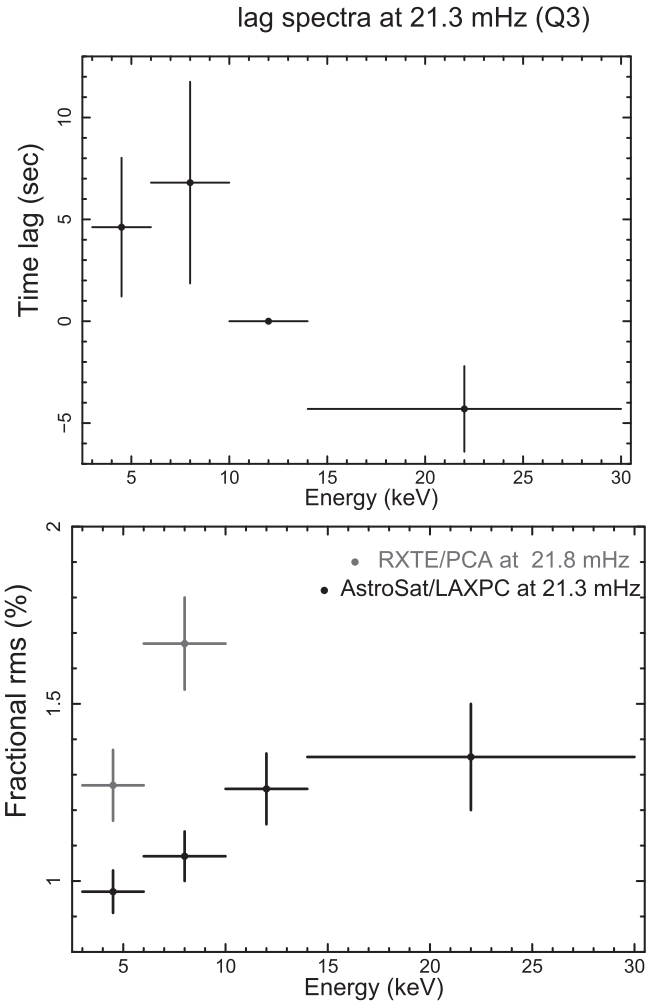

Figure 9. Top panel shows time-lag spectra as a function of photon energy as observed from *AstroSat*/LAXPC at the QPO frequency of 21.3 mHz (Q3). While calculating the time delay in different energy bands, 10.0–14.0 keV is considered to be the reference band. A soft-lag behavior (soft photons lag hard photons) is observed. Such a study with *RXTE*/PCA is not possible since QPO is not detected above 10 keV. The bottom panel shows background-corrected fractional rms (%) of the mHz QPO from *AstroSat*/LAXPC (shown in black) and *RXTE*/PCA (shown in gray) as a function of photon energy. Since QPO is not detected above 10 keV with *RXTE*/PCA, the rms spectral study with PCA is restricted to 10 keV.

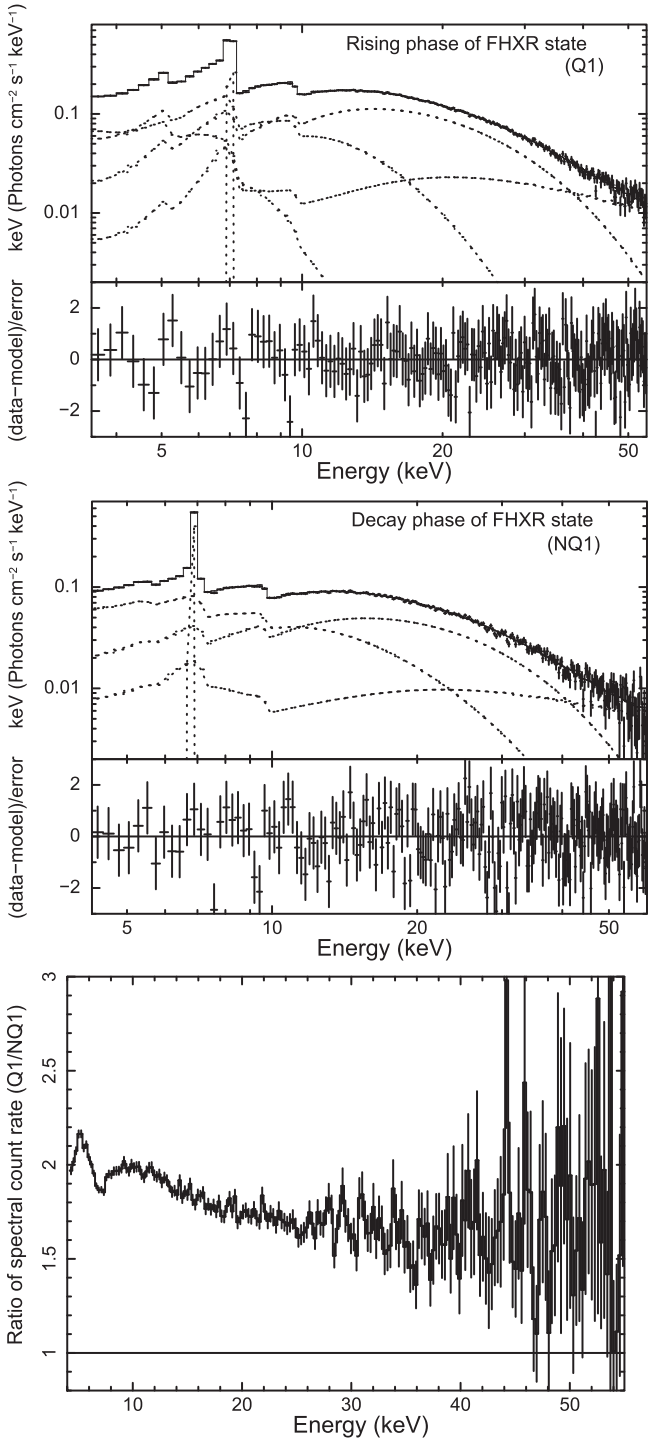

Figure 10. Top panel shows the energy spectra of Cyg X-3 along with its residual obtained during the rising phase when fitted with a model consisting of a disk blackbody emission, thermal Comptonization, thermal Bremsstrahlung emission, disk reflection, a narrow emission line, and edges. Middle panel shows the fitted energy spectra of Cyg X-3 along with the residual during decay phase using the same model. Bottom panel shows the ratio of the background-subtracted rising phase and decay phase spectral count rate as a function of photon energy. Up to 50 keV, the ratio is found to be significantly higher than 1. Such behavior of the ratio spectrum indicates a change in spectral shape between the rising and decay phase spectra.

be boosted by the presence of the in-phase oscillation of the electron density of a high optical depth corona (Lee & Miller 1998) formed by the accreted wind. This is also supported by the fact that at higher energy the thermal Comptonization component dominates the spectrum as observed from the top and middle panel in Figure 10, while the fractional rms of ∼21 mHz QPO increases with the photon energy as shown in the bottom panel of Figure 9.

One key result obtained from LAXPC is the time-lag at different energy bands. This is possible owing to the high efficiency of LAXPC at higher energy (Yadav et al. 2016a). Figure 9 shows that relatively softer photons lag relatively harder photons with a timescale of up to ∼5 s. Our spectral analysis shows that energy spectra during QPO detections have optically thick plasma from where Compton scatterings are taking place. Therefore, it is possible that high energy photons undergo Compton down-scattering to produce low-energy photons. Due to the optically thick medium, soft photons may undergo larger down-scatterings within a scattering medium of the size of 10–12 s. Therefore, with such a timescale and spectral nature, it is possible that softer photons

will be delayed compared to harder photons of the order of 5 s. Investigating further into the origin of soft-lag is presently out of the scope of the present work.

We thank the referee for constructive suggestions that improved the quality of the manuscript. We acknowledge the strong support from Indian Space Research Organization (ISRO) in various aspects of instrument building, testing, software development, and mission operation during PV and GT observational phases. We acknowledge the support of the TIFR central workshop during the fabrication and the testing of the payload.

ORCID iDs

Mayukh Pahari https://orcid.org/0000-0002-5900-9785
H M Antia https://orcid.org/0000-0001-7549-9684
Jai Verdhan Chauhan https://orcid.org/0000-0002-5736-1654

References

Agrawal, P. C. 2006, AdSpR, 38, 2989
Altamirano, D., Belloni, T., Linares, M., et al. 2011, ApJL, 742, L17
Altamirano, D., & Strohmayer, T. 2012, ApJL, 754, L23
Antia, H. M., Yadav, J. S., Agrawal, P. C., et al. 2017, arXiv:1702.08624
Axelsson, M., Larsson, S., & Hjalmarsdotter, L. 2009, MNRAS, 394, 1544
Belloni, T., Klein-Wolt, M., Meńdez, M., van der Klis, M., & van Paradijs, J. 2000, A&A, 355, 271
Berger, M., & van der Klis, M. 1994, A&A, 292, 175
Bodaghee, A., Tomsick, J. A., Pottschmidt, K., et al. 2013, ApJ, 775, 98
Choudhury, M., & Rao, A. R. 2004, ApJL, 616, L143
Dickey, J. M. 1983, ApJL, 273, L71
Dickey, J. M., & Lockman, F. J. 1990, ARA&A, 28, 215
Dunn, R., Fender, R., Ko:rding, E., Belloni, T., & Cabanac, C. 2010, MNRAS, 403, 61
Fender, R. P., Belloni, T. E., & Gallo, E. 2004, MNRAS, 355, 1105
Fender, R. P., Hanson, M. M., & Pooley, G. G. 1999, MNRAS, 308, 473
Giacconi, R., Gorenstein, P., Gursky, H., & Waters, J. R. 1967, ApJL, 148, L119
Holt, S. S., Boldt, E. A., & Serlemitsos, P. J. 1976, Natur, 260, 592
Jahoda, K., Markwardt, C. B., Radeva, Y., et al. 2006, ApJS, 163, 401
Kitamoto, S., Miyamoto, S., Matsui, W., & Inoue, H. 1989, PASJ, 41, 81
Koljonen, K. I. I., Hannikainen, D. C., & McCollough, M. L. 2011, MNRAS, 416, L84
Koljonen, K. I. I., Hannikainen, D. C., McCollough, M. L., Pooley, G. G., & Trushkin, S. A. 2010, MNRAS, 406, 307
Koljonen, K. I. I., McCollough, M. L., Hannikainen, D. C., & Droulans, R. 2013, MNRAS, 429, 1173
Leach, R. W., Murray, S. S., Schreier, E. J., et al. 1975, ApJ, 199, 184
Lee, H. C., & Miller, G. S. 1998, MNRAS, 299, 479
Manchanda, R. K. 2002, JApA, 23, 197
Manchanda, R. K., & Rao, A. R. 1993, AdSpR, 13, 335
Mioduszewski, Amy J., Rupen, Michael P., Hjellming, Robert M., et al. 2001, ApJ, 553, 766
Misra, R., Yadav, J. S., Verdhan Chauhan, J., et al. 2017, ApJ, 835, 195
Molnar, L. A., Reid, M. J., & Grindlay, J. E. 1988, ApJ, 331, 494
Molteni, D., Rapisarda, M., Robba, N. R., & Scarsi, L. 1980, A&A, 87, 88
Neilsen, J., Remillard, R. A., & Lee, J. C. 2011, ApJ, 737, 69
Nowak, M. A., Wilms, J., & Dove, J. B. 1999, ApJ, 517, 355
Pahari, M., Yadav, J. S., & Bhattacharyya, S. 2014, ApJ, 783, 141
Parsignault, D. R., Gursky, H., Kellogg, E. M., et al. 1972, NPhS, 239, 123
Predehl, P., & Schmitt, J. H. M. M. 1995, A&A, 239, 889
Rao, A. R., Agrawal, P. C., & Manchanda, R. K. 1991, A&A, 241, 127
Remillard, R. A., & McClintock, J. E. 2006, A&A, 44, 49
Ross, R. R., & Fabian, A. C. 2005, MNRAS, 358, 211
Schalinski, C. J., Johnston, K. J., Witzel, A., et al. 1995, ApJ, 447, 752
Singh, K. P., Tandon, S. N., Agrawal, P. C., et al. 2014, Proc. SPIE, 9144, 91441
Singh, N. S., Naik, S., Paul, B., et al. 2002, A&A, 392, 161
Suto, Y., & Iso, K.-I. 1980, Ap&SS, 115, 243
Szostek, A., & Zdziarski, A. A. 2004, arXiv:astro-ph/0401265
Szostek, A., & Zdziarski, A. A. 2008, MNRAS, 386, 593
Szostek, A., Zdziarski, A. A., & McCollough, M. L. 2008, MNRAS, 388, 1001
van der Klis, M., & Bonnet-Bidaud, J. M. 1981, A&A, 95, L5
van der Klis, M., & Bonnet-Bidaud, J. M. 1989, A&A, 214, 203
van der Klis, M., & Jansen, F. A. 1985, Natur, 313, 768
Vaughan, S. 2005, A&A, 431, 391
Vilhu, O., Hakala, P., Hannikainen, D. C., McCollough, M., & Koljonen, K. 2009, A&A, 501, 679
Willingale, R., King, A. R., & Pounds, K. A. 1985, MNRAS, 215, 295
Vilhu, O., Hjalmarsdotter, L., Zdziarski, A. A., et al. 2003, A&A, 411, L405
Yadav, J. S., Agrawal, P. C., Antia, H. M., et al. 2016b, Proc. SPIE, 9905, 99051
Yadav, J. S., Misra, R., Verdhan Chauhan, J., et al. 2016a, ApJ, 833, 27
Zdziarski, Andrzej A., Misra, Ranjeev, & Gierliński, Marek 2010, MNRAS, 402, 767